Carbon 247 (2026) 121017

Contents lists available at ScienceDirect

Carbon

journal homepage: www.elsevier.com/locate/carbon

Low-entropy skeleton domain engineering for broadband electromagnetic wave absorption

Huiliang Wen [a], Xiaojun Li [a], Xiaomeng Jiang [a], Yunlong Jing [a], Tong Huang [b], Xuliang Nie [c,*], Chongbo Liu [b,**]

[a] Jiangxi Hongzhou Vocational College, Fengcheng, 331100, China
[b] School of Environmental and Chemical Engineering, Nanchang Hangkong University, Nanchang, 330063, China
[c] College of Chemistry & Materials, Jiangxi Agricultural University, Nanchang, 330045, China

ARTICLE INFO

Keywords:
Low entropy
Structure modulation
Boron doping
Electromagnetic wave absorption
Multifunctionality

ABSTRACT

With the rapid development of electronic technology, the issues of electromagnetic radiation and interference have become increasingly critical, making the design of high-performance electromagnetic wave absorbing (EMWA) materials a research focus. In this study, two types of boron-based covalent organic framework (COF) aerogel precursors containing $FeNi_{10}$ (FN) have been prepared via non-directional and directional freeze-drying, followed by pyrolysis to yield disordered and ordered FN@BCA composite aerogels, respectively. The disordered FN@BCA-7 exhibits a reflection loss (*RL*) of −27.68 dB at 2 mm thickness and an effective absorption bandwidth (EAB, $RL \leq -10$ dB) of 5.68 GHz at 1.85 mm. The construction of low-entropy carbon skeleton domains further improves impedance matching. Consequently, the ordered FN@BCA-7D achieves an *RL* of −38.2 dB at 2.2 mm and an EAB of 6.88 GHz at 2.5 mm. Density functional theory calculations reveal that the introduction of electron-deficient boron atoms enhances electrical conductivity and polarization loss. In multifunctional applications, FN@BCA-7D demonstrates a radar cross-section reduction of 31.31 dB m^2 and excellent thermal insulation. Furthermore, the gradient metamaterial design extends the EAB to 37.62 GHz. Overall, this study introduces a promising strategy for developing EMWA materials with broadband absorption, high efficiency, multifunctionality, and environmental adaptability.

1. Introduction

With the rapid advancement of modern technologies, the widespread use of electromagnetic equipment and the intensification of electromagnetic signals have led to increasingly severe electromagnetic pollution. High-intensity electromagnetic radiation not only disrupts the normal operation of precision electronic devices but may also adversely affect the nervous and immune systems when the human body is exposed to elevated radiation levels for extended periods [1–4]. In this context, the development of electromagnetic wave absorbing (EMWA) materials with lightweight structures and broadband absorption has become a critical task in mitigating electromagnetic pollution. At the same time, practical application scenarios often involve complex environments that demand not only strong EMWA, but also admirable environmental adaptability. This has shifted the research focus from optimizing single EMWA performance to achieving multifunctional integration [5,6].

Covalent organic framework (COF) materials have recently attracted attention in the EMWA field owing to their structural and functional advantages [7,8]. Their abundant pores and high surface area extend the propagation path of electromagnetic waves (EMWs), increase the interaction time between EMWs and the absorber, and facilitate multiple scattering. For example, Zhu et al. successfully synthesized hollow core–shell Fe/Fe_3O_4@porous carbon composites via calcinating Fe_3O_4@-COF. At a thickness of 1.8 mm, the material achieved a reflection loss (*RL*) of −50.05 dB and an effective absorption bandwidth (EAB, $RL \leq 10$ dB) of 5.20 GHz [9], underscoring the key role of the porous structure of COFs in enhancing EMWA performance.

In addition, COFs often contain polar heteroatoms, which break the symmetry of internal charge distribution, form electric dipoles, and generate dipole polarization under alternating electromagnetic fields, thereby increasing polarization loss [10,11]. Doping strategies can

* Corresponding author.
** Corresponding author.
E-mail addresses: xuliangnie123@163.com (X. Nie), cbliu2002@163.com (C. Liu).

https://doi.org/10.1016/j.carbon.2025.121017
Received 15 September 2025; Received in revised form 20 October 2025; Accepted 29 October 2025
Available online 30 October 2025

further enhance conductivity and introduce heterogeneous atomic defects, improving both conductivity and polarization losses, as reported by Xia et al. [12]. For instance, Ning et al. prepared gradient nitrogen-doped graphene with nitrogen contents of 0 wt% (pure rGO), 3.7 wt% (NG-100), and 6.86 wt% (NG-240) by hydrothermal synthesis. Compared with undoped graphene, NG-100 achieved an *RL* of −55 dB at 3.2 mm, five times greater than that of pure rGO [13]. However, limited research has explored the doping role of weakly electronegative boron atoms in EMWA materials.

Meanwhile, Peng et al. reported that combining dielectric and magnetic materials to achieve synergistic effects remained a widely recognized principle for designing broadband EMWA systems [14]. For example, Zhao et al. synthesized hollow carbon fiber composites containing CoFe alloy via electrospinning and high-temperature pyrolysis (CF@HCF). Compared with pure hollow carbon fibers (HCFs), CoFe@HCF achieved an *RL* of −50.04 dB at 2.4 mm and extended the EAB from 3.52 to 6.06 GHz [15], confirming that introducing magnetic components is an effective strategy to supplement magnetic losses, optimize impedance matching, and overcome performance bottlenecks.

Aerogels further address the contradiction between high EMWA efficiency and low weight through their highly porous structures. Moreover, they exhibit multifunctional properties such as thermal insulation and mechanical robustness, expanding their applicability [16–18]. For example, Gao et al. constructed a spider-web-inspired composite aerogel via ball-milling-assisted mono-dispersion and self-assembly technology, which demonstrated both excellent EMWA performance and outstanding elasticity and thermal insulation [19]. Similarly, Liu et al. fabricated MXene/graphene oxide aerogels (SMGAs) using direct ink writing (DIW) three-dimensional (3D) printing, which not only exhibited strong EMWA ability but also exceptional compressive strength, withstanding 36,000 times their own weight without significant deformation [20]. These examples have illustrated the potential of aerogels in broadening the application scenarios of EMWA materials.

According to Li et al., the state of phase distribution is another crucial factor influencing EMWA performance [21]. From a thermodynamic perspective, the random arrangement of components typically increases system entropy, leading to irregular electron transport pathways, reduced conductivity, and weakened conductivity losses. In contrast, guiding materials into ordered network structures lowers entropy, promotes charge transport, and enhances conductivity losses. For example, Liang et al. employed directional freeze-drying combined with hydrazine vapor reduction to construct an ordered honeycomb-like Ni/MXene/RGO aerogel, which achieved an EAB of ~5.0 GHz at 2.5 mm. Conversely, disordered samples with skeleton aggregation and disrupted networks exhibited insufficient polarization loss and poor EMWA [22]. Similarly, Xu et al. fabricated honeycomb-shaped carbon aerogels embedded with Co nanoparticles via directional freeze casting and carbonization. Their ordered porous structure, high conductivity, and abundant interfaces generated a synergistic effect, achieving a wide EAB of 4.02 GHz and an *RL* of −45.02 dB at 1.5 mm [23].

Building on these insights, the present study employs B-based COFs as precursors, $FeNi_{10}$ alloy as the magnetic component, and aerogels as the macro-scale carrier, while regulating entropy through ordered structural design. The resulting NF@BCA composites achieve broadband EMWA, strong energy loss, and excellent thermal insulation, thereby offering a new design pathway for multifunctional EMWA materials suited to complex environments.

2. Experimental section

2.1. Synthesis of $FeNi_{10}$ (FN) alloy

$FeNi_{10}$ alloy was synthesized by a hydrothermal method. Briefly, 0.065 g of $FeCl_3{\cdot}6H_2O$ and 0.57 g of $NiCl_2{\cdot}6H_2O$ were dissolved in 48 mL of deionized water. Subsequently, 0.38 g of NaOH and 5 mL of hydrazine hydrate were added under stirring. The mixture was then transferred into a Teflon-lined autoclave and heated at 120 °C for 10 h. The resulting products were collected via magnetic separation, washed several times with deionized water, and dried at 60 °C.

2.2. Synthesis of FN@COF

To prepare FN@COF, 0.224 g of 2,3,6,7,10,11-hexahydroxytriphenyl (HHTP), 0.177 g of 1,4-phenyldiboronic acid (PBBA), 0.08 g of FN alloy, and 0.45 mL of methanol were dissolved in 86 mL of a co-solvent mixture of 1,4-dioxane and mesitylene (4:1, v/v). The solution was sonicated until homogeneous, then transferred to a Teflon-lined high-pressure reactor, and heated at 90 °C for 20 h. After cooling to room temperature, the precipitate was collected by centrifugation, washed three times with toluene and acetone, and dried under vacuum for 12 h.

2.3. Synthesis of FN@BCA

For the synthesis of FN@BCA, 0.15 g of sodium carboxymethylcellulose (CMC-Na) and 0.08 g of FN@COF were dissolved in 5 mL of deionized water and stirred to form a homogenous gel. Subsequently, liquid nitrogen was utilized as a cryogen during the freezing process, inducing the growth of ice crystals in a bottom-to-top direction in the directional freezing samples. The samples were subsequently freeze-dried overnight at −66 °C and 30 Pa, and then pyrolyzed under N_2 at 600, 700, or 800 °C at a heating rate of 2 °C/min. The resulting products were denoted as FN@BCA-6D, FN@BCA-7D, and FN@BCA-8D (directional), as well as FN@BCA-6, FN@BCA-7, FN@BCA-8 (non-directional).

2.4. Characterization

The morphology of the samples was examined using field-emission scanning electron microscopy (FE-SEM, FEI Nova NanoSEM450) and transmission electron microscopy (TEM, Talos F200X). High-resolution TEM (HRTEM) was employed to investigate detailed microstructural features. Crystalline phase composition and elemental distribution were characterized by powder X-ray diffraction (PXRD, Bruker D8 Advance A25) and energy-dispersive spectroscopy (EDS). X-ray photoelectron spectroscopy (XPS, Thermo Fisher Scientific ESCALAB Xi+) was used to analyze surface chemical states and elemental valence. Raman spectroscopy (LabRAM HR800) with a 532 nm laser and a scanning range of 800–2000 cm^{-1} was applied to evaluate graphitization degree. Electromagnetic parameters in the frequency range of 2–18 GHz were measured using a vector network analyzer (Agilent PNA N5224A) via the coaxial line method. Thermal insulation performance of FN@BCA-7D was further evaluated using a thermal imaging camera (FLIR E85).

3. Results and discussion

The synthesis route of FN@BCA aerogels is illustrated in Fig. 1. First, organic monomers containing boronic acid and hydroxyl groups undergo condensation to form a COF skeleton with a periodic porous structure. During this step, FN alloy particles are uniformly encapsulated within the COF, remaining embedded during subsequent carbonization to contribute magnetic loss. With CMC-Na serving as a crosslinking agent, polar groups and hydrogen bonds connect the COF and CMC-Na molecules, yielding a stable 3D network structure. Through contrasting modes of directional and non-directional ice crystals during freeze-drying, ordered low-entropy and disordered high-entropy aerogels are obtained. Finally, the freeze-dried gels are pyrolyzed at different temperatures, producing a series of FN@BCA aerogels.

The morphology of the FN@BCA-D composites was examined by SEM and TEM. As illustrated in Fig. 2a–f, FN alloy particles are tightly encapsulated by the BCA matrix, preventing agglomeration. Compared with FN@BCA-7 (Fig. S2), FN@BCA-7D exhibits a more ordered

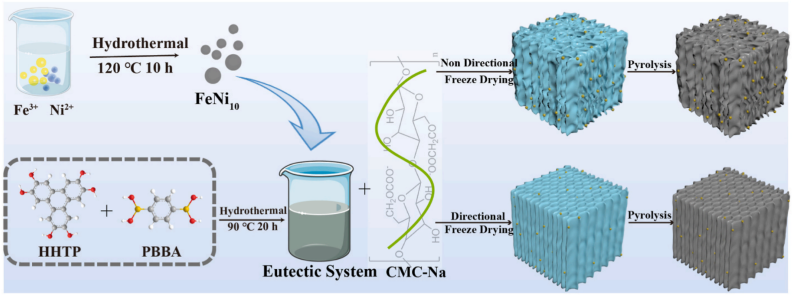

Fig. 1. Synthesis process of FN@BCA aerogels

network structure. However, raising the calcination temperature to 800 °C (FN@BCA-8D) causes partial collapse of the porous framework, leading to the loss of regular reticular features. The HRTEM image of FN@BCA-7D (Fig. 2g) clearly reveals the formation of a heterogeneous interface between the FN alloy and surrounding carbon layer, which promotes interfacial polarization. Lattice fringes are evident in Fig. 2h–j, with an average spacing of 0.217 nm, slightly larger than that of the Ni (111) plane (0.204 nm). This expansion arises from Fe incorporation into the Ni lattice, which increases the average interplanar distance [24]. Moreover, point defects are observed in Fig. 2k, which interact with EMWs and generate dipole polarization effects [25,26]. EDS mapping (Fig. 2l) further confirms that FN alloy particles are uniformly distributed and firmly anchored in the BCA matrix.

The XRD patterns of FN@BCA-D are displayed in Fig. 2m. Three characteristic diffraction peaks at 44.34°, 51.67°, and 76.09° correspond to the (111), (200), and (220) planes of pure Ni (JCPDS #03-65-0380), respectively. For FN@BCA-D, these peaks shift to 44.50°, 51.85°, and 76.37°, indicating that Fe incorporation perturbs the regular Ni lattice, causing peak deviation. In addition, the diffraction peak near 26° corresponds to the (002) crystal plane of carbon, whereas the absence of impurity peaks demonstrates the high crystallinity of the synthesized composites.

The XPS survey spectrum of FN@BCA-7D (Fig. S3) confirms the presence of C, O, B, Ni, and Fe elements. High-resolution spectra of B 1s and Ni 2p are shown in Fig. 2n–o. The B 1s peaks at 188.9 and 192.2 eV correspond to the B–C bond and BCO_2 species [27,28], respectively. Boron incorporation optimizes the electronic structure, introduces additional polarization centers, and thus enhances polarization losses. In the Ni 2p region, peaks at 855.5 and 873.39 eV are assigned to Ni $2p_{3/2}$ and Ni $2p_{1/2}$, while satellite peaks appear at 861.4 and 878.2 eV [29]. These findings are consistent with PXRD and EDS analyses, collectively confirming the successful synthesis of FN@BCA composites.

The EMWA performance of materials is primarily evaluated by *RL* and EAB [30,31]. FN@BCA and FN@BCA-D composites are synthesized at calcination temperatures of 600, 700, and 800 °C, and their *RL* and EAB values are displayed in Fig. 3a–f. Among the non-directional samples, FN@BCA-6 and FN@BCA-8 exhibit poor absorption, with *RL* values of only −4.5 dB and −7.6 dB, respectively. In contrast, FN@BCA-7 achieves an *RL* of −27.68 dB at 2 mm thickness and an EAB of 5.68 GHz at 1.85 mm. Similarly, the directional samples of FN@BCA-6D and FN@BCA-8D shows weak absorption ($RL < -10$ dB), whereas FN@BCA-7D delivers the best performance, with an *RL* of −38.2 dB at 2.2 mm and an EAB of 6.88 GHz at 2.5 mm.

Raman spectroscopy was further employed to elucidate why calcination temperature strongly influenced performance (Fig. 3g). The peaks at ~1350 and ~1580 cm^{-1} correspond to the D band (defective carbon, I_D) and G band (graphitized carbon, I_G) [32], respectively. The I_D/I_G ratios for FN@BCA-6D, FN@BCA-7D, and FN@BCA-8D were 1.12, 0.66, and 0.44, respectively, showing a decreasing trend with higher calcination temperatures. This indicates a progressive increase in graphitization degree. Further quantitative analysis of graphite domain size (L_a), average defect distance (L_d), and defect density (n_d) is performed using Equations S8–S10 [33–35]. As shown in Fig. S5a, L_a increases from 17.16 nm to 43.69 nm with rising temperature, mirroring the enhancement in graphitization. Similarly, L_d increase from 11.50 nm to 18.35 nm, while n_d decrease from 2.28×10^{11} to 1.02×10^{11} cm^{-2}. These results confirm that higher calcination temperatures reduce defect density and promote graphitization, thereby influencing EMWA performance.

This phenomenon can be explained by hybrid orbital theory. During pyrolysis, the $2p_z$ orbitals of carbon atoms are oriented perpendicular to the XY plane, overlap to form π-bonds. Every six carbon atoms generate delocalized large π-bonds which are only weakly bound electronically. As the pyrolysis temperature increases, more sp^2 bonds are formed, enabling additional $2p_z$ orbitals to contribute more electrons to these delocalized π-domains. This process greatly increases the carrier concentration. Moreover, adjacent π-domains provide high-speed channels for electron migration [36]. Consequently, the degree of graphitization of the sample progressively increases with higher temperatures. However, the influence of graphitization-induced changes in electrical conductivity on EMWA performance is a double-edged sword. At low conductivity (e.g., samples calcined at 600 °C), conduction losses are insufficient. At excessively high conductivity (e.g., 800 °C), strong interactions with the electromagnetic field give rise to the "skin effect," which induces currents and reflects incident EMWs [37].

Impedance matching, defined by $|Z_{in}/Z_0| = 1.0$, indicates that incident EMWs are completely absorbed by the material [38,39]. A comparison of impedance matching plots for FN@BCA-7 and FN@BCA-7D (Fig. 3h–i) reveals that FN@BCA-7D achieves superior impedance matching over a broader frequency range. This observation is further supported by Smith plots (Fig. S6), where the purple area represents the effective absorption region [40,41]. Optimal impedance matching requires that as many input impedance (Z_{in}) points as possible fall within this region. Notably, at 2.50 mm thickness, FN@BCA-7D shows more Z_{in} points inside the purple region than FN@BCA-7 at 1.85 mm, confirming that the construction of low-entropy skeletal domains enhances impedance matching.

The dielectric constant of the composites (Fig. 4a and b) decreases with increasing frequency, which is attributed to polarization hysteresis: carriers struggle to keep pace with rapid changes in high-frequency electromagnetic fields [42]. FN@BCA-7, FN@BCA-7D, FN@BCA-8, and FN@BCA-8D all exhibit distinct resonance peaks, signifying that strong polarization loss enhances EMWA performance. In contrast, FN@BCA-6 and FN@BCA-6D exhibit lower dielectric constants and weaker electromagnetic responses. The permeability curves (Fig. 4c and d) show that μ' and μ'' represent magnetic storage and dissipation capacities, respectively. All samples demonstrate low permeability, indicating that magnetic loss contributes minimally to attenuation. Interestingly, FN@BCA-6 and FN@BCA-6D display negative μ'' values in certain frequency bands, suggesting that their magnetic losses cannot

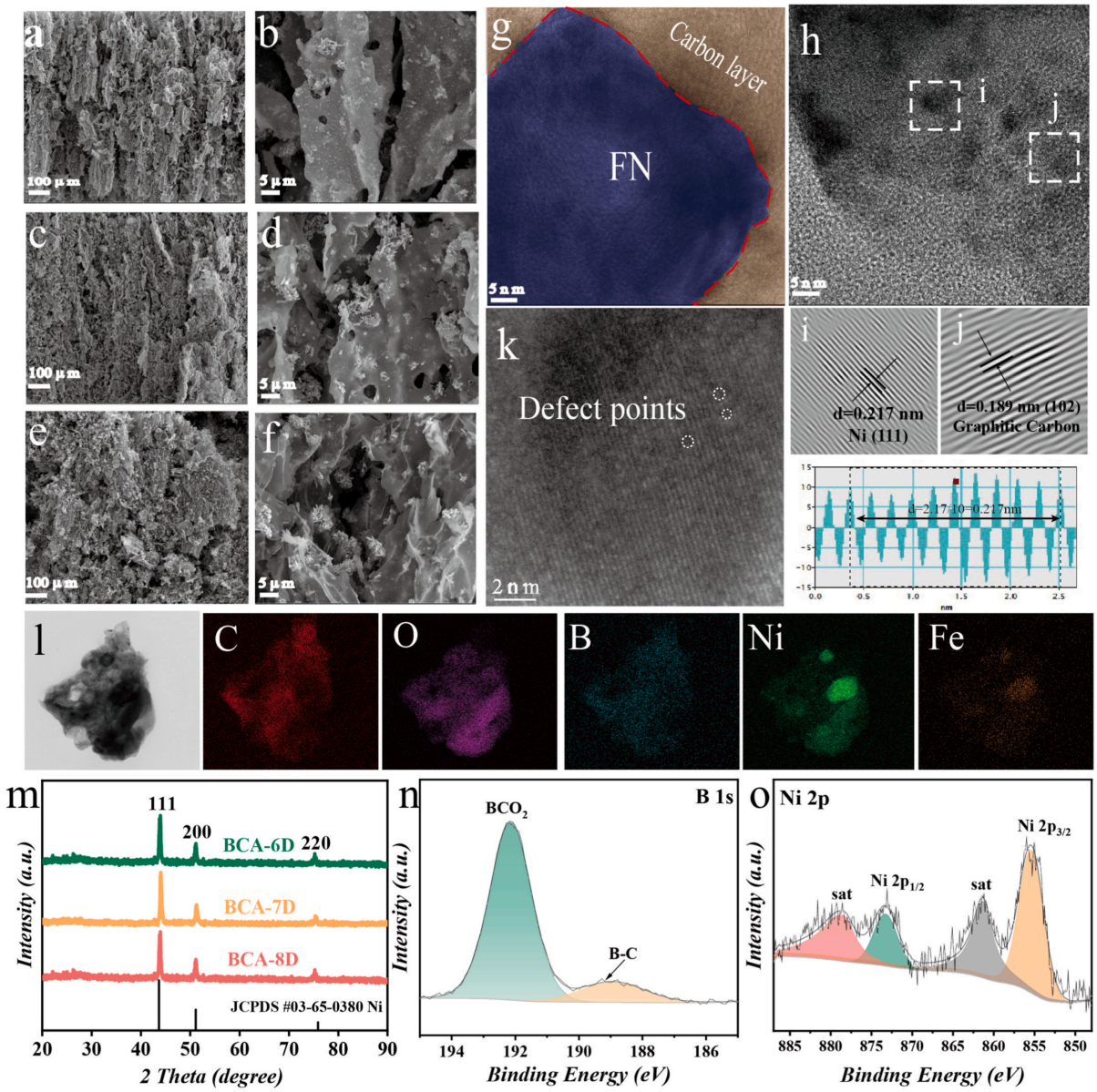

Fig. 2. SEM images of (a–b) FN@BCA-6D, (c–d) NF@BCA-7D, (e–f) FN@BCA-8D. (g–k) HRTEM images of FN@BCA-7D, (l) EDS mapping of FN@BCA-7D. (m) XRD pattern of FN@BCA. High-resolution XPS spectra of (n) B 1s and (o) Ni 2p for FN@BCA-7D.

compensate for radiated magnetic energy [43]. This effect has also been reported in other magnetic materials [44,45]. Fig. S7 shows the eddy current loss coefficient (C_0) of the samples. In the low-frequency range, the C_0 curve exhibits significant variation, indicating that magnetic loss in this range is primarily attributed to natural and exchange resonance. In the high-frequency range, the C_0 curve changes gradually and approaches a straight line, suggesting that magnetic loss at high frequencies is dominated by eddy current loss. Although small resonance peaks with minor fluctuations appear in the C_0 curves, no distinct absorption peaks are observed in the *RL* curves at the corresponding frequencies, indicating that the contribution of the magnetic loss mechanism to EMWA is relatively weak.

To further analyze loss mechanisms, dielectric ($\tan\delta_\varepsilon$) and magnetic ($\tan\delta_\mu$) loss tangents were calculated (Fig. 4i). The $\tan\delta_\varepsilon$ values are considerably higher than $\tan\delta_\mu$, demonstrating that dielectric loss dominates FN@BCA composites. Dielectric loss originates mainly from conduction and polarization losses, where alternating electric fields induce heat via energy conversion. To quantify the contribution of polarization, polarization loss percentages ($\varepsilon_p''/\varepsilon''$) for FN@BCA-7 and FN@BCA-7D are evaluated (Fig. 4e–f). These are visualized as small spheres: as frequency increases, their color deepens and size enlarges, indicating enhanced polarization loss with frequency.

Dielectric loss is closely associated with polarization relaxation behavior. In polarization loss analysis, Debye relaxation theory

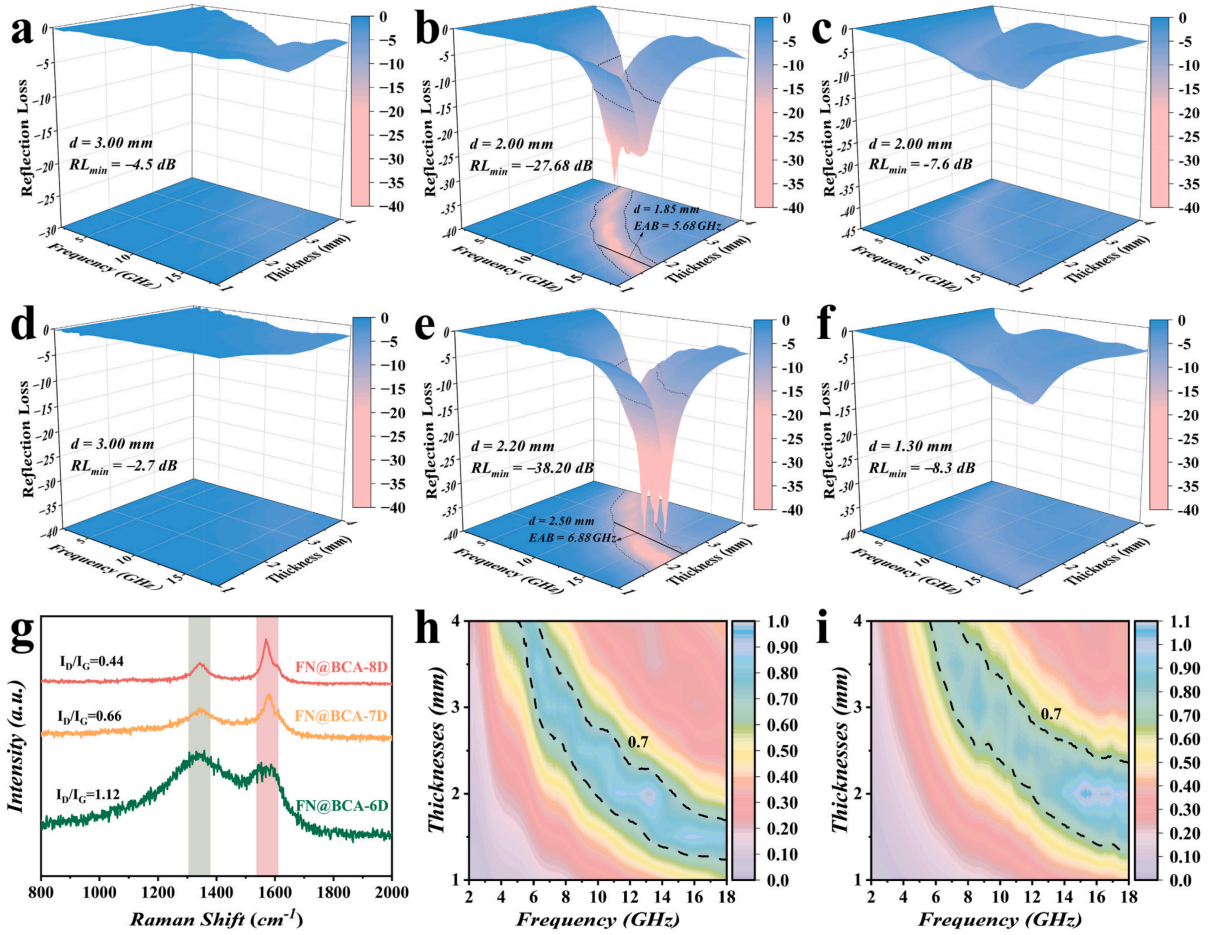

Fig. 3. 3D RL plots of (a) FN@BCA-6, (b) FN@BCA-7, (c) FN@BCA-8, (d) FN@BCA-6D, (e) FN@BCA-7D, and (f) FN@BCA-8D. (g) Raman spectra of FN@BCAD. Impedance matching plots of (h) FN@BCA-7 and (i) FN@BCA-7D.

describes the polarization loss of polar molecules in alternating electric fields and can be expressed by Equation S4. According to this theory, each semicircle in a Cole-Cole curve corresponds to an independent Debye relaxation process. The Cole-Cole curves of FN@BCA-7 and FN@BCA-7D are shown in Fig. S8. Both exhibit multiple semicircular structures, indicating the presence of multiple polarization relaxation behaviors. The Cole–Cole curve of FN@BCA-7D displays a longer tail than that of FN@BCA-7, which is attributed to the more favorable conductive transmission path in FN@BCA-7D for conductive loss. The multiple semicircles and trailing characteristics of the Cole-Cole curve confirm the synergistic mechanism of polarization and conduction loss in the composite materials. The linear relationship between ε' and ε''/f is shown in Fig. 4g–h, where the slope represents polarization behavior [46]. The fitted curves confirm that both FN@BCA-7 and FN@BCA-7D exhibit multipolarization relaxation behaviors, consistent with the results from the Cole-Cole curves. This relaxation behavior can be attributed to three mechanisms: i) intrinsic polarization of the BCA substrate, ii) interfacial polarization arising from heterogeneous interfaces between FN and BCA, and iii) abundant polarization centers within the composite.

To gain deeper insight into the electromagnetic loss mechanism of FN@BCA materials, density of states (DOS), partial density of states (PDOS), and charge density difference (CDD) analyses were performed using density functional theory (DFT) based on a refined structural model. The DOS plot (Fig. 4j) highlights the atom orbital contributions to EMWA. At the Fermi level, the DOS is predominantly governed by the p-orbitals of carbon, which form delocalized π-bonds. These π-bonds facilitate ability to transfer and transition of electrons, thereby enhancing conductivity loss. The carbon skeleton forms the primary pathway for charge carriers, and the p-orbital hybridization of boron and oxygen redistributes the DOS near the Fermi level, which modulates the conductivity loss. Moreover, the p-orbitals of boron and oxygen contribute to the formation of polarization centers, further strengthening polarization loss. The CDD map (Fig. S9) illustrates the charge distribution in the material. Boron, oxygen and carbon possess different electronegativities, which generates asymmetric charge. Under high-frequency electromagnetic fields, these asymmetric charges undergo oscillation and rotation, markedly enhancing the dipole polarization effect.

To evaluate the potential of these materials for practical applications, the radar wave attenuation capabilities of FN@BCA-7 and FN@BCA-7D were investigated under far-field conditions using radar cross-section (RCS) simulations (Fig. 5b–c) [47]. A two-layer square plate is modeled using CST simulation software, consisting of a perfect electric conductor (PEC, 200 × 200 mm, 2 mm thick) coated with FN@BCA-7 (2 mm thick) or FN@BCA-7D (2.2 mm thick). The

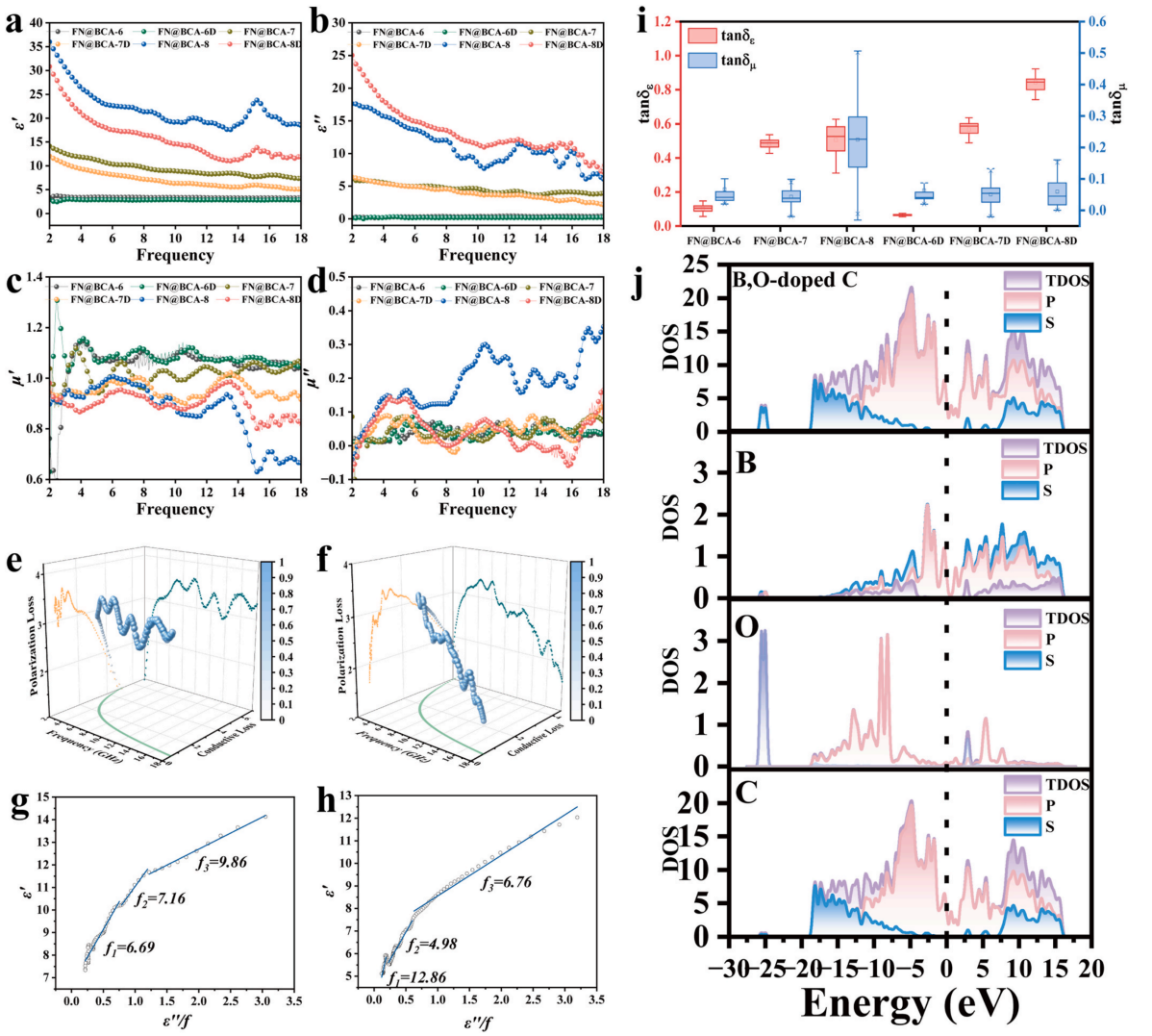

Fig. 4. (a–d) Electromagnetic parameters. 3D polarization percentage of (e) FN@BCA-7 and (f) FN@BCA-7D. Polarization relaxation behavior of (g) FN@BCA-7 and (h) FN@BCA-7D. (i) $tan\delta_\varepsilon$ and $tan\delta_\mu$ of FN@BCA and FN@BCA-D. (j) Total DOS and PDOS plots.

simulations are conducted at 13.28 and 15.28 GHz. As expected, the bare PEC exhibits negligible dissipation capacity for radar waves. However, when coated with FN@BCA-7 or FN@BCA-7D, the scattering values are substantially reduced at a 0° incidence angle. Notably, FN@BCA-7D achieves a maximum RCS reduction of 31.31 dB m^2, outperforming FN@BCA-7 (22.90 dB m^2), which is fully consistent with their relative EMWA performance.

Thermal insulation performance enables materials to retain excellent EMWA properties even under extreme conditions such as high and low temperatures [48]. To evaluate the thermal insulation capability of FN@BCA-7D, the sample was placed on a heating table at 140 °C, and its surface temperature was recorded every 10 min. As shown in Fig. 5d, the temperature increased from 54 °C to 74 °C during the first 10 min. After 40 min, the temperature stabilized at 76 °C, maintaining a difference of ~64 °C between the heating plate and the material surface. This considerable thermal barrier effect is attributed to the highly porous structure of the aerogel, which traps air and significantly suppresses heat conduction and radiation. Overall, FN@BCA-7D demonstrates outstanding thermal insulation performance, fulfilling the requirements for operation in harsh environments.

To further broaden the EAB, a metamaterial with a truncated-pyramid architecture was designed by stacking three layers of FN@BCA-7D and integrating a honeycomb perforated structure. Based on the 1/4 wavelength principle, this gradient metamaterial provides multiple electromagnetic response mechanisms. By tuning the gradient thickness, multiple EMW interference absorption peaks are generated, thereby enhancing overall EMWA performance. As shown in Fig. 5e, the FN@BCA-7D-based gradient metamaterial achieves an exceptionally wide EAB of 37.62 GHz (2–40 GHz) and an RL_{min} of −39.93 dB at 2.84 GHz.

To assess angle dependance, simulations were conducted under different incident angles. Notably, the metamaterial still maintains an EAB of 35.8 GHz at a high incident angle of 70°, confirming its insensitivity to the incident EMW angle. Therefore, this structural design

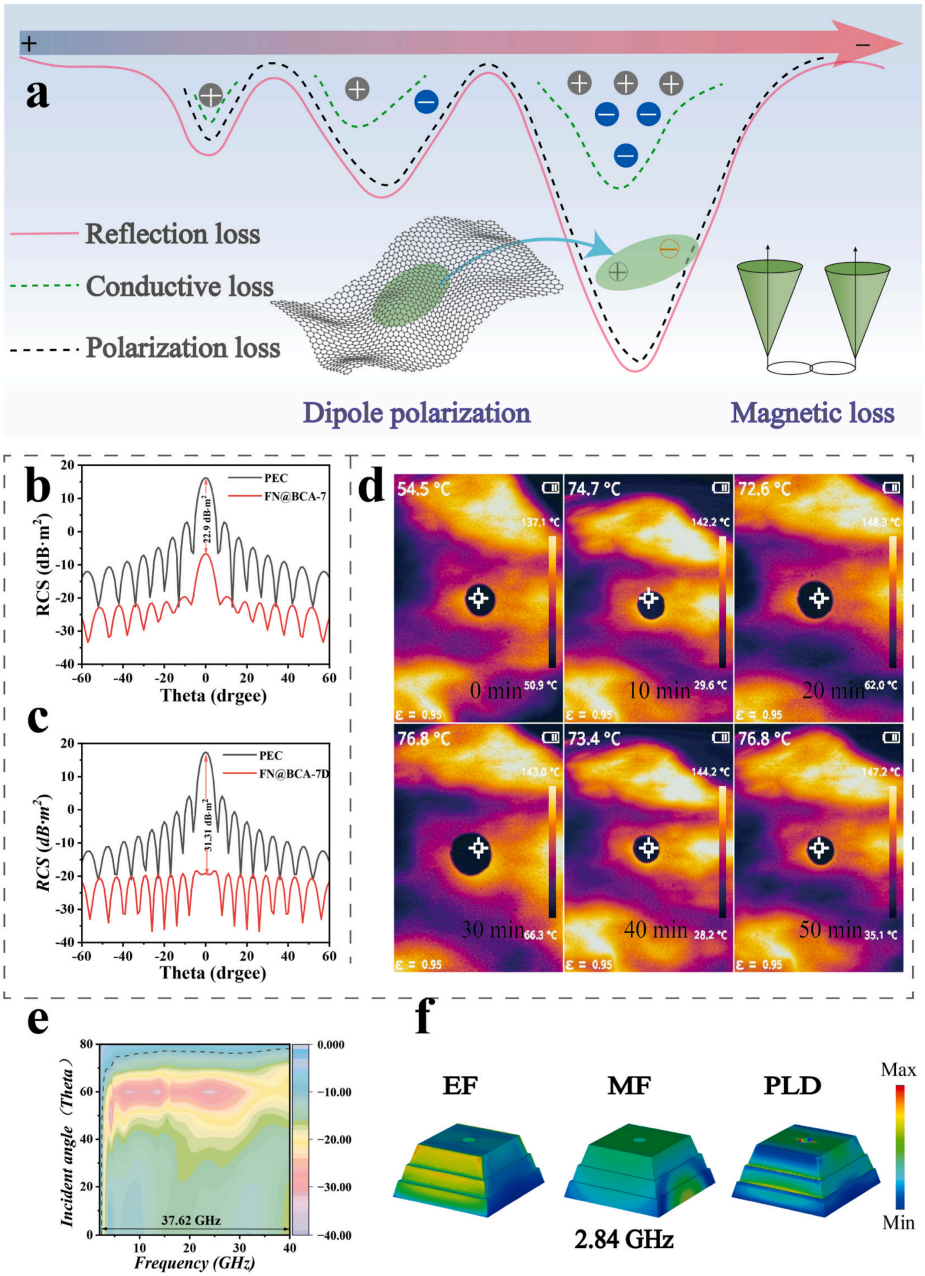

Fig. 5. (a) EMWA mechanism of FN@BCA composites. (b–c) Radar stealth performance. (d) Thermal insulation performance of FN@BCA-7D. (e–f) Gradient metamaterial design.

provides a comprehensive optimization of material performance. The loss mechanisms of the gradient metamaterial were further analyzed through electromagnetic simulations of the electric field, magnetic field, and power loss density distributions at 2.84 GHz (Fig. 5f). The electric field is concentrated at the pyramid edges, while the magnetic field is localized near the base of the structure, indicating strong low-frequency EMW absorption by the underlying material. The power loss density is particularly pronounced at the honeycomb walls and the pyramid base, suggesting that the gradient geometry induces diffraction and secondary scattering, which synergistically enhance EMWA. Thus, the rational gradient design effectively overcomes the inherent limitations of EMWA materials, achieving ultra-broadband adsorption.

4. Conclusions

In this study, FN@BCA-D aerogels were successfully prepared via a low-entropy construction strategy, which effectively optimized impedance matching and broadened the electromagnetic response bandwidth.

The modulation of graphite domain size was shown to significantly influence the electromagnetic parameters and EMWA properties: an appropriate graphite domain size ensured good electrical conductivity while preventing excessive EMW reflection. In addition, the incorporation of boron introduced abundant dipole polarization centers, serving as a major source of polarization loss, as further confirmed by DFT calculations. The embedded FN alloy contributed magnetic losses that worked synergistically with dielectric losses, enhancing overall EMW attenuation. Through directional architecture engineering, FN@BCA-7D achieved a wide effective absorption bandwidth of 6.88 GHz, with its far-field attenuation ability validated by RCS simulations. Moreover, FN@BCA-7D demonstrated outstanding thermal insulation, ensuring stable performance under extreme environmental conditions. Overall, this study provided a versatile strategy for designing multifunctional, high-performance EMWA materials and offered valuable insights for their practical deployment in complex application scenarios.

CRediT authorship contribution statement

Huiliang Wen: Writing – original draft, Methodology, Investigation, Formal analysis, Data curation, Conceptualization. **Xiaojun Li:** Writing – original draft, Formal analysis, Data curation. **Xiaomeng Jiang:** Validation, Investigation, Funding acquisition. **Yunlong Jing:** Resources, Investigation, Funding acquisition. **Tong Huang:** Writing – original draft, Data curation. **Xuliang Nie:** Writing – review & editing. **Chongbo Liu:** Writing – review & editing, Supervision, Project administration, Funding acquisition.

Declaration of competing interest

The authors declare that they have no known competing financial interests or personal relationships that could have appeared to influence the work reported in this paper.

Acknowledgement

This work was supported by the National Natural Science Foundation of China (22265021), Science and Technology Research Project of Jiangxi Provincial Department of Education (GJJ2409506 and GJJ2409507). The authors extend their gratitude to Ms. Li Wenjuan (from Scientific Compass www.shiyanjia.com) for providing invaluable assistance with the XPS analysis and MJEditor (http://www. mjeditor.com) for their linguistic assistance during the preparation of this manuscript.

Appendix A. Supplementary data

Supplementary data to this article can be found online at https://doi.org/10.1016/j.carbon.2025.121017.

References

[1] Y. Zhang, C. Tang, Y. Song, S. Zhang, Z.H. Hang, X. Zhang, et al., High-entropy alloy nanoparticles combined with an SiC coating synergistically boost the electromagnetic shielding performance of a carbon nanotube sponge, J. Mater. Chem. A 12 (2024) 13498–13509.
[2] T.T. Liu, L.Y. Li, P. Gao, L. Li, M.S. Cao, High-entropy electromagnetic functional materials: from electromagnetic genes to materials design, Mater. Sci. Eng. R Rep. 164 (2025) 100982.
[3] J. Hu, L. Jiang, L. Jia, J. Jin, A. Wu, X. Zhang, Novel carbonitriding process of high-entropy alloys using mechanochemical process for obtaining excellent high-frequency electromagnetic properties, Carbon 228 (2024) 119406.
[4] Z.Z. Zhang, Y. Kong, J.M. Zhang, J. Hou, M.S. Cao, X.X. Wang, Recent progress of microwave absorption motivated by metal single atoms anchored on two-dimensional materials, Carbon 235 (2025) 120095.
[5] L.Y. Li, M. Zhang, M. Jiang, L.H. Gao, Z. Ma, M.S. Cao, et al., High entropy ceramics for electromagnetic functional materials, Adv. Funct. Mater. 35 (2025) 2416673.
[6] J.Y. Zong, H.Z. Zhai, H.Z. Guan, Z.Z. Wang, M.S. Cao, W.Q. Cao, et al., Host-Guest engineered electromagnetic fabrics with controllable polarization-conduction network for multispectral stealth and wireless actuation, Adv. Funct. Mater. (2025) e07277, https://doi.org/10.1002/adfm.202507277.
[7] G. Li, R. Tan, B. Gao, X. Liu, M. Zhang, P. Chen, et al., PB@COF-derived core–shell Fe/Fe_3O_4/C composites with excellent electromagnetic wave absorption performance for the entire Ku band, Chem. Eng. J. 504 (2025) 159010.
[8] Z. Deng, L. Wang, B. Peng, L. Ye, Z. Li, Z. Shi, et al., Optimization of electromagnetic wave absorption properties by formation of magnetoelectric synergistic effect of COF-derived carbon composite Fe/Fe_3C, Chem. Eng. J. 505 (2025) 159457.
[9] X. Zhu, Y. Dong, F. Pan, Z. Xiang, Z. Liu, B. Deng, et al., Covalent organic framework-derived hollow core-shell Fe/Fe_3O_4@porous carbon composites with corrosion resistance for lightweight and efficient microwave absorption, Compos. Commun. 25 (2021) 100731.
[10] G. Shao, Y. Yang, S. Jia, G. Yu, X. Nan, C. Li, et al., Covalent organic framework-amplified polarization loss in ultralight schottky heterojunction aerogels for low-frequency electromagnetic wave absorption, Adv. Funct. Mater. (2025) e16078, https://doi.org/10.1002/adfm.202516078.
[11] Y. Li, X. Gao, M. Wang, Y. Gao, D. Jiang, Annealed covalent organic framework thin films for exceptional absorption of ultrabroad low-frequency electromagnetic waves, Small 18 (2022) 2205400.
[12] Y. Xia, W. Gao, C. Gao, A review on graphene-based electromagnetic functional materials: electromagnetic wave shielding and absorption, Adv. Funct. Mater. 32 (2022) 2204591.
[13] M. Ning, B. Kuang, L. Wang, J. Li, H. Jin, Correlating the gradient nitrogen doping and electromagnetic wave absorption of graphene at gigahertz, J. Alloys Compd. 854 (2021) 157113.
[14] H. Peng, D. Zhang, Z. Xie, S. Lu, Y. Liu, F. Liang, Recent advances in structural design of carbon/magnetic composites and their electromagnetic wave absorption applications, Small 21 (2025) 2408570.
[15] Y. Zhao, L. Wang, Z. Liu, J. Ren, H. Wang, J. Hu, et al., Simple synthesis of hollow CoFe carbon fiber composites with enhanced heterogeneous interfaces and impedance matching for broadband microwave absorption, J. Mater. Sci. Technol. 238 (2025) 178–190.
[16] S. Wang, X. Zhang, S. Hao, J. Qiao, Z. Wang, L. Wu, et al., Nitrogen-doped magnetic-dielectric-carbon aerogel for high-efficiency electromagnetic wave absorption, Nano-Micro Lett. 16 (2024) 16.
[17] Y. Li, X. Liu, X. Nie, W. Yang, Y. Wang, R. Yu, et al., Multifunctional organic–inorganic hybrid aerogel for self-cleaning, heat-Insulating, and highly efficient microwave absorbing material, Adv. Funct. Mater. 29 (2019) 1807624.
[18] Q. Qu, Y. Zhou, Q. Yang, J. Cao, Y. Liu, X. Qi, S. Jiang, et al., Lignin-derived lightweight carbon aerogels for tunable epsilon-negative response, Adv. Sci. 11 (2024) 2401767.
[19] C. Gao, D. Gou, G. Huang, Z. Zhang, J. Wei, F. Gao, et al., Spiderweb-structured aerogels with high-efficiency microwave absorption and multifunctionality, Nano Energy 138 (2025) 110863.
[20] X. Liu, W. Ma, Z. Qiu, T. Yang, J. Wang, X. Ji, et al., Manipulation of impedance matching toward 3D-printed lightweight and stiff MXene-based aerogels for consecutive multiband tunable electromagnetic wave absorption, ACS Nano 17 (2023) 8420–8432.
[21] L. Li, F. Pan, H. Guo, H. Jiang, X. Wang, K. Yao, et al., Tailored magnetic spatial confinement with enhanced polarization and magnetic response for electromagnetic wave absorption, Small 20 (2024) 2402564.
[22] L. Liang, Q. Li, X. Yan, Y. Feng, Y. Wang, H. Zhang, et al., Multifunctional magnetic Ti_3C_2Tx MXene/Graphene aerogel with superior electromagnetic wave absorption performance, ACS Nano 15 (2021) 6622–6632.
[23] J. Xu, X. Zhang, Z. Zhao, H. Hu, B. Li, C. Zhu, et al., Lightweight, fire-retardant, and anti-compressed honeycombed-like carbon aerogels for thermal management and high-efficiency electromagnetic absorbing properties, Small 17 (2021) 2102032.
[24] L. Kral, A. Chesalkin, J. Cermak, P. Roupcova, E. Prusov, Influence of Fe on the hydrogen storage properties of LaCeNi alloys, Langmuir 39 (2023) 6061–6068.
[25] Z. Qiu, X. Liu, T. Yang, J. Wang, Y. Wang, W. Ma, et al., Synergistic enhancement of electromagnetic wave absorption and corrosion resistance properties of high entropy alloy through lattice distortion engineering, Adv. Funct. Mater. 34 (2024) 2400220.
[26] B. Zhao, Z. Yan, Y. Du, L. Rao, G. Chen, Y. Wu, et al., High-entropy enhanced microwave attenuation in titanate perovskites, Adv. Mater. 35 (2023) 2210243.
[27] Z. Zhou, X. Zhang, L. Xing, J. Liu, A. Kong, Y. Shan, Copper-assisted thermal conversion of microporous covalent melamine-boroxine frameworks to hollow B, N-codoped carbon capsules as bifunctional metal-free electrode materials, Electrochim. Acta 298 (2019) 210–218.
[28] S. Umezawa, T. Douura, K. Yoshikawa, Y. Takashima, M. Yoneda, K. Gotoh, et al., Supercapacitor electrode with high charge density based on boron-doped porous carbon derived from covalent organic frameworks, Carbon 184 (2021) 418–425.
[29] R.Z. Hu, X. He, Y.Q. Luo, C.B. Liu, S.Y. Liu, X.T. Lv, et al., Biomimetic multi-interface design of raspberry-like absorbent: Gd-doped $FeNi_3$@Covalent organic framework derivatives for efficient electromagnetic attenuation, Small Methods 9 (2025) 2401299.
[30] N. Wang, Y. Wang, Z. Lu, R.R. Cheng, L.Q. Yang, Y.F. Li, Hierarchical core-shell FeS_2/Fe_7S_8@C microspheres embedded into interconnected graphene framework for high-efficiency microwave attenuation, Carbon 202 (2023) 254–264.
[31] J. Lin, Y. Peng, J. Luo, Z. Xiong, J. Huang, X. Zeng, et al., One-click to 3D: helical carbon nanotube-mediated MXene hierarchical aerogel with layer spacing engineering for broadband electromagnetic wave absorption, Small Methods 9 (2025) 2401665.

[32] L. Shi, W. Liu, F. Zhao, R. Liu, Y. Sun, C. Dong, et al., Tailoring the dual precursors coupled hard carbon by embedding the pitch-derived graphitic domains to achieve high-performance sodium storage, J. Power Sources 596 (2024) 234093.
[33] J. Tao, L. Xu, H. Jin, Y. Gu, J. Zhou, Z. Yao, et al., Selective coding dielectric genes based on proton tailoring to improve microwave absorption of MOFs, Adv. Powder Mater. 2 (2023) 100091.
[34] Y. Li, R. Liu, X. Pang, X. Zhao, Y. Zhang, G. Qin, et al., Fe@C nanocapsules with substitutional sulfur heteroatoms in graphitic shells for improving microwave absorption at gigahertz frequencies, Carbon 126 (2018) 372–381.
[35] Y. Yang, J. Cheng, F. Pan, S. Lu, X. Wang, L. Cai, et al., Phragmites-derived magnetic carbon fiber with hollow assembly architecture toward full-covered effective bandwidth at Ku band, Carbon 213 (2023) 118228.
[36] J. Tao, K. Zou, J. Zhou, H. Wu, L. Xu, J. Wang, et al., Phenolic multiple kinetics-dynamics and discrete crystallization thermodynamics in amorphous carbon nanostructures for electromagnetic wave absorption, Nat. Commun. 15 (2024) 10337.
[37] Y. Zhou, Y. Wang, S. Qiu, W. Zhao, S. Wang, H. Bao, Z. Wen, et al., Microscopic response mechanism of epsilon-negative and epsilon-near-zero metacomposites, Research 8 (2025) 556.
[38] J. Lin, H.L. Wen, Z.B. Feng, R.Z. Hu, L.P. Wu, C.B. Liu, et al., Anion injection in dielectric ecosystems to construct dual built-in electric fields for efficient electromagnetic response, Adv. Funct. Mater. (2025) 2505381.
[39] M. Liu, H. Wu, Y. Wang, J. Ren, D.A. Alshammari, H.E.A. Elsalam, et al., Flexible cementite/ferroferric oxide/silicon dioxide/carbon nanofibers composite membrane with low-frequency dispersion weakly negative permittivity, Adv. Compos. Hybrid Mater. 6 (2023) 217.
[40] J. Tao, J. Zhou, Z. Yao, J. Wang, L. Xu, X. Tao, et al., Multi-field coupled motion induces electromagnetic wave absorbing property regeneration of elastomer in marine environment, Adv. Funct. Mater. 34 (2024) 2310640.
[41] Z. Feng, C. Liu, X. Li, G. Luo, N. Zhai, R. Hu, et al., Designing electronic structures of multiscale helical converters for tailored ultrabroad electromagnetic absorption, Nano-Micro Lett. 17 (2025) 20.
[42] P.T. Xie, H.Y. Li, B. He, F. Dang, J. Lin, R.H. Fan, et al., Bio-gel derived nickel/carbon nanocomposites with enhanced microwave absorption, J. Mater. Chem. C 6 (2018) 8812–8822.
[43] F. Pan, X. Wu, D. Batalu, W. Lu, H. Guan, Assembling of low-dimensional aggregates with interlaminar electromagnetic synergy network for high-efficient microwave absorption, Adv. Powder Mater. 2 (2023) 100100.
[44] L. Liu, N. He, T. Wu, P.B. Hu, G.X. Tong, Co/C/Fe/C hierarchical flowers with strawberry-like surface as surface plasmon for enhanced permittivity, permeability, and microwave absorption properties, Chem. Eng. J. 355 (2019) 103–108.
[45] S. Lin, J. Lin, Z. Xiong, X. He, X. Li, C. Liu, et al., Micro-helical Ni_3Fe chain encapsulated in ultralight MXene/C aerogel to realize multi-functionality: radar stealth, thermal insulation, fire resistance, and mechanical properties, Chem. Eng. J. 492 (2024) 152248.
[46] H. Wu, Z. Zhang, C. Wang, K.M. Abualnaja, H.M. Abo-Dief, Q. Hou, et al., Radio-frequency broadband epsilon-near-zero response in biocompatible silver nanoparticles/polystyrene films with three-dimensional honeycomb-like superstructures, Adv. Compos. Hybrid Mater. 6 (2023) 206.
[47] Y. Chen, M. Chen, H. Lei, L. Song, R. Zhang, H. Li, et al., Microwave-assisted synthesis of high-performance TaC nanorods for enhanced electromagnetic wave absorption, J. Adv. Ceram. 14 (2025) 9221130.
[48] N.P. Li, D.F. Zhang, R.H. Yang, H. Gao, H.Y. Zhang, One-step pyrolyzed $Co_6Mo_6C_2$/Mo_2C/Co/C foam integrating multiple schottky heterojunctions for simultaneous thermal insulation and electromagnetic wave absorption, Carbon 244 (2025) 120681.